

# Quantum theory of three-junction flux qubit with non-negligible loop inductance: Towards scalability

T. L. Robertson,\* B. L. T. Plourde,† P. A. Reichardt, T. Hime, C.-E. Wu,‡ and John Clarke  
*Department of Physics, 366 LeConte Hall, University of California, Berkeley, California 94720-7300, USA*  
 (Received 6 January 2006; published 30 May 2006)

The three-junction flux qubit (quantum bit) consists of three Josephson junctions connected in series on a superconducting loop. We present a numerical treatment of this device for the general case in which the ratio  $\beta_Q$  of the geometrical inductance of the loop to the kinetic inductance of the Josephson junctions is not necessarily negligible. Relatively large geometric inductances allow the flux through each qubit to be controlled independently with on-chip bias lines, an essential consideration for scalability. We derive the three-dimensional potential in terms of the macroscopic degrees of freedom, and include the possible effects of asymmetry among the junctions and of stray capacitance associated with them. To find solutions of the Hamiltonian, we use basis functions consisting of the product of two plane wave states and a harmonic oscillator eigenfunction to compute the energy levels and eigenfunctions of the qubit numerically. We present calculated energy levels for the relevant range of  $\beta_Q$ . As  $\beta_Q$  is increased beyond 0.5, the tunnel splitting between the ground and first excited states decreases rapidly, and the device becomes progressively less useful as a qubit.

DOI: [10.1103/PhysRevB.73.174526](https://doi.org/10.1103/PhysRevB.73.174526)

PACS number(s): 03.67.Lx, 85.25.Cp, 85.25.Dq

## I. INTRODUCTION

A superconducting loop interrupted by a single Josephson tunnel junction was originally proposed for the investigation of macroscopic quantum coherence.<sup>1</sup> At a flux bias of  $(n + 1/2)\Phi_0$  ( $\Phi_0 \equiv h/2e$ ,  $n$  is an integer) and appropriate device parameters, this device has two degenerate states corresponding to opposite senses of supercurrent circulating around the loop. Coherent tunnel coupling leads to superpositions of these two circulating current states with distinct energy levels. As the flux bias is moved away from the degeneracy point, the ground and first excited states approach the clockwise and anticlockwise circulating current states. The first experimental evidence for the quantum superposition of two macroscopic flux states was realized in this device.<sup>2</sup> In these experiments the junction critical current needed to be adjusted with a second magnetic flux. Furthermore, the tunnel coupling between the ground states in the potential was vanishingly small, so that the measured superpositions were formed between highly excited states in the two wells, adding complexity to the manipulation of the quantum state of the device. Nonetheless, the formation of superpositions of states through the tunnel coupling enables this single-junction device to behave as a flux quantum bit (“qubit”). Subsequently, a second kind of flux qubit was proposed, consisting of three Josephson junctions in series interrupting the loop.<sup>3</sup> In the case of the three-junction flux qubit, it is possible to have a substantial tunnel coupling between the ground states in the two degenerate potential wells; this coupling is determined by the relative sizes of the junctions which are set during fabrication, thus eliminating the need to tune the critical currents precisely. In addition, the loop inductance of the three-junction flux qubit can cover a wide range, while still providing a reasonable tunnel coupling. For either kind of qubit, a superconducting quantum interference device (SQUID) is used to measure the flux generated by the circulating current, thus detecting the qubit state.

The splitting between the qubit ground and first excited state is typically several gigahertz, so that the flux qubit can

be controlled with microwave pulses. Several groups have used microwave spectroscopy to map out the splitting by measuring the resonance frequency as the qubit flux bias is varied.<sup>4-6</sup> Furthermore, for a fixed flux bias in the qubit, one can manipulate the flux qubit state coherently to generate Rabi oscillations, Ramsey fringes, and echoes.<sup>6-8</sup> To produce the desired energy levels, flux qubits generally have small junction capacitances, typically a few femtofarads. As a result, the junctions are submicron, with typical linewidths of a few hundred nanometers. The Al-AlOx-Al junctions used to date have been produced with masks made with electron-beam lithography and a double-angle shadow evaporation technique.<sup>9</sup> Nominally identical junctions often vary significantly in area and thus in critical current and capacitance, and may have non-negligible stray capacitances. Thus, it is important that a complete theory for the three-junction flux qubit be able to account for such asymmetries and parasitic capacitances.

An important challenge to implementing an array of flux qubits is the requirement for a scalable flux biasing scheme. Although nanofabrication techniques allow one to place many qubits on a single chip, it is essential to be able to bias each qubit independently<sup>6</sup> while maintaining an appropriate flux in the readout SQUID(s) to ensure high sensitivity. Thus, each qubit requires its own on-chip flux bias line, coupled to a current supply, as does each readout SQUID. In practice, these flux lines need not be independent since one can sum the flux bias currents in combinations determined by the various mutual inductances between the flux lines and the qubits and SQUIDs to bias any given device with the desired flux. However, to supply a flux of the order of  $\Phi_0$  to a given element, its mutual inductance with the flux bias line must be large enough to ensure a bias current that is not too high. For example, a bias current of 1 mA requires a mutual inductance of 2 pH with a given loop to generate a flux  $\Phi_0$  in it. This requirement, in turn, implies that the loop inductance must be tens or even hundreds of picohenries. Schemes to entangle qubits may also benefit from relatively large induc-

tances, which increase the coupling energy.<sup>10</sup> Such inductances are much larger than those used in early experiments, in which the geometrical inductance  $L_Q$  (a few picohenries) was negligible compared with the Josephson inductances. Thus, it is necessary to develop a theory that is valid for arbitrary ratios of the geometric and Josephson inductances.

The initial theoretical study of the energy levels arising from the macroscopic degrees of freedom of the three-junction flux qubit reduced the problem to two dimensions by neglecting the qubit loop inductance.<sup>11</sup> Subsequently, the effect of small, but nonzero, loop inductance was included perturbatively.<sup>12</sup> Another treatment involved expansions in powers of the inductive terms to produce an effective Hamiltonian for evaluating interaction energies between flux qubits.<sup>13</sup> The inductive energy for three-junction flux qubits was considered by You *et al.*,<sup>14</sup> but the calculations were still performed in the two-dimensional approximation, which neglects the contribution to the action from the third degree of freedom. To calculate accurately the effect of larger loop inductances, that is when the inductive energy arising from the persistent current in the qubit is comparable to the Josephson energy, one must consider the full three-dimensional system.

In this paper, we present a theory for the three-junction flux qubit in which we solve the full three-dimensional problem. In Sec. II, we derive expressions for the potential energy in terms of the macroscopic degrees of freedom; we include the effects of loop inductance, junction asymmetry, and stray capacitance. In Sec. III, we obtain the Hamiltonian for the three-junction flux qubit, and in Sec. IV, we solve the Hamiltonian in a rapidly convergent series expansion to find the energy levels. Section V contains some concluding remarks.

## II. THREE-DIMENSIONAL POTENTIAL

The three-junction flux qubit shown in Fig. 1 consists of three Josephson junctions, one with a somewhat smaller critical current than the other two, embedded in a superconducting loop. To determine the energetically favorable configurations of the qubit, one considers the potential energy of the system as a function of the macroscopic degrees of freedom. The potential energy has inductive and Josephson contributions  $U=U_I+U_J$ . The inductive contribution is

$$U_I=L_Q J_Q^2/2, \quad (1)$$

where  $J_Q$  is the current circulating in the qubit. The Josephson contribution, which provides the nonlinearity necessary for a qubit, is

$$U_J=\Phi_0/(2\pi)[I_{01}(1-\cos\gamma_1)+I_{02}(1-\cos\gamma_2)+I_{03}(1-\cos\gamma_3)]. \quad (2)$$

Here the  $I_{0i}$  are the critical currents of the three junctions and the  $\gamma_i$  are the phase differences across them ( $i=1,2,3$ ). The phase differences and the circulating current are connected through the fluxoid condition

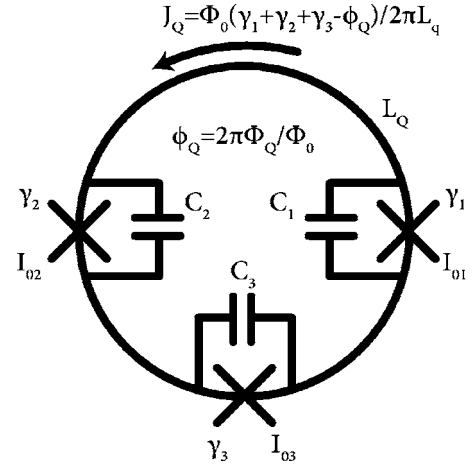


FIG. 1. Schematic of three-junction flux qubit with loop inductance  $L_Q$ , reduced applied flux  $\phi_Q$ , circulating current  $J_Q$ , and phase differences  $\gamma_i$  across Josephson junctions of critical current  $I_{0i}$ .

$$\gamma_1 + \gamma_2 + \gamma_3 = \phi_Q + 2\pi L_Q J_Q / \Phi_0, \quad (3)$$

where  $\phi_Q = 2\pi\Phi_Q/\Phi_0$  is the flux bias applied to the qubit in units of phase. This constraint can be used to eliminate  $J_Q$  from Eq. (1) and express  $U$  in terms of only the  $\gamma_i$ .

In Fig. 2 we show three contours of constant potential energy in the three-dimensional space spanned by the  $\gamma_i$ . We see that far away from the plane defined by  $\gamma_1 + \gamma_2 + \gamma_3 = \phi_Q$  the inductive energy dominates and the surfaces of constant potential energy approach parallel planes (blue contours). When the inductive energy is small the periodic nature of  $U_J$  becomes apparent, manifest in Fig. 2 as the closed red contours which enclose multiple local minima.

To facilitate analysis of the potential, we introduce the dimensionless parameters

$$\beta_Q = \frac{2\pi L_Q}{\Phi_0} \left( \frac{1}{I_{01}} + \frac{1}{I_{02}} + \frac{1}{I_{03}} \right)^{-1}, \quad (4)$$

which characterizes the relative importance of Josephson and geometric inductances,

$$\alpha_Q = 2I_{03}/(I_{01} + I_{02}), \quad (5)$$

which describes the relative size of the small junction, and

$$\kappa_Q = (I_{01} - I_{02})/(I_{01} + I_{02}), \quad (6)$$

which characterizes asymmetry between the two large junctions.

The structure of the potential becomes clearer if we rotate it into a coordinate system defined by a set of variables aligned with the plane of zero inductive energy. We define the total phase variable

$$\gamma_s = \alpha_Q(\phi_Q - \gamma_1 - \gamma_2 - \gamma_3)/(1 + 2\alpha_Q), \quad (7)$$

which runs normal to the plane of zero inductive energy. We decompose the in-plane coordinates into a symmetric mode

$$\gamma_s = \frac{1}{2(1 + 2\alpha_Q)} [2\alpha_Q(\gamma_3 - \phi_Q) - \gamma_1 - \gamma_2] \quad (8)$$

and an antisymmetric mode

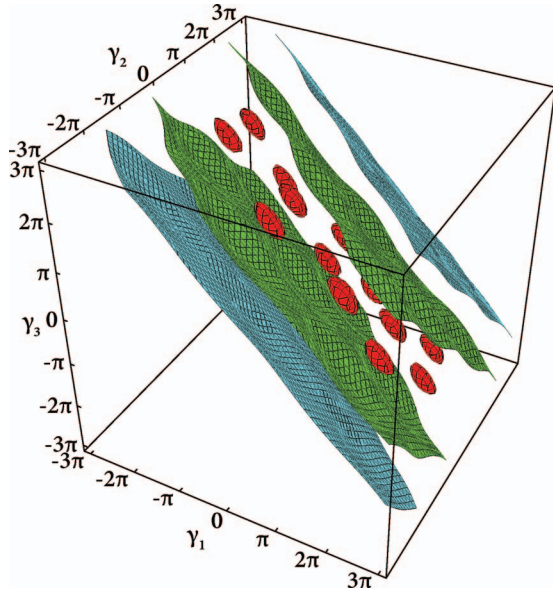


FIG. 2. (Color) Three-junction flux qubit potential. Three contours of potential energy [ $U=1.4E_J$  (red),  $U=10E_J$  (green), and  $U=30E_J$  (blue)] are shown. Parameters are  $\alpha_Q=0.8$ ,  $\beta_Q=0.4$ ,  $\kappa_Q=0$ , and  $\phi_Q=\pi$ .

$$\gamma_a = (\gamma_1 - \gamma_2)/2. \quad (9)$$

After subtracting off a constant, we find the Josephson energy

$$U_J = -E_J[(1 + \kappa_Q)\cos(\gamma_a - \gamma_s - \gamma_t) + (1 - \kappa_Q)\cos(\gamma_a + \gamma_s + \gamma_t) + \alpha_Q\cos(2\gamma_s + \phi_Q - \gamma_t/\alpha_Q)], \quad (10)$$

where  $E_J = (I_{01} + I_{02})\Phi_0/4\pi$ . The inductive energy depends on  $\gamma_t$  and is given by

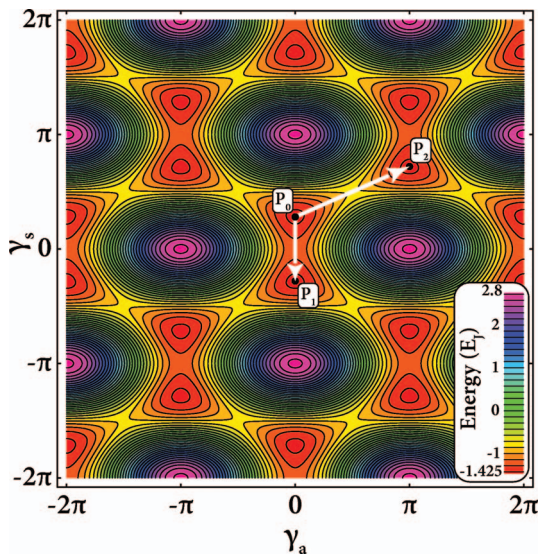


FIG. 3. (Color) Slice through  $\gamma_t=0$  of three-junction flux qubit potential. Parameters are  $\alpha_Q=0.8$ ,  $\beta_Q=0.01$ ,  $\kappa_Q=0$ , and  $\phi_Q=\pi$ .

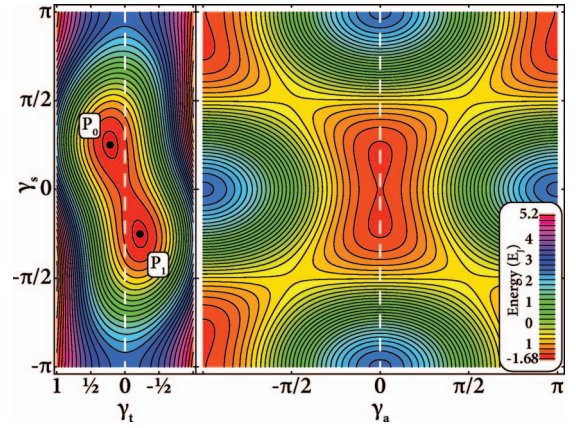


FIG. 4. (Color) Unit cell of a larger inductance flux qubit. Slices are shown through both the  $\gamma_t$ - $\gamma_s$  plane and the  $\gamma_a$ - $\gamma_s$  plane, which coincide along the dotted line. Parameters are  $\alpha_Q=0.6$ ,  $\beta_Q=0.4$ ,  $\kappa_Q=0$ , and  $\phi_Q=\pi$ .

$$U_l = E_J \frac{(1 + 2\alpha_Q)^2(1 - \kappa_Q^2)}{2\alpha_Q\beta_Q(1 + 2\alpha_Q - \kappa_Q^2)} \gamma_t^2. \quad (11)$$

Considering first the small  $\beta_Q$  regime, we see that  $U_l$  dominates, so that solutions of minimum potential energy will have  $\gamma_t \approx 0$ . We thus reduce the three-dimensional problem to a two-dimensional one. This is the regime which has been studied in previous treatments of the three-junction flux qubit.<sup>11</sup> When the qubit is biased at  $\Phi_0/2$  ( $\phi_Q=\pi$ ), we see the array of degenerate local minima shown in Fig. 3. Closer inspection reveals that the minima come in pairs separated by a barrier, the intracell barrier, such as those marked by the points  $P_0$  and  $P_1$ . A larger barrier separates neighboring pairs of minima, the intercell barrier, as indicated along the arrow from  $P_0$  to  $P_2$ .

At  $\phi_Q=\pi$ , the potential energies associated with the minima  $P_0$ ,  $P_1$ , and  $P_2$  are degenerate. This degeneracy is principally lifted by the tunneling matrix element connecting  $P_0$  and  $P_1$ , resulting in a ground state that is a symmetric superposition of states localized at  $P_0$  and  $P_1$ , and an excited state that is a corresponding antisymmetric superposition. However, the much smaller tunneling matrix element connecting  $P_0$  and  $P_2$  also serves to lift the degeneracy, giving states that are symmetric and antisymmetric superpositions of states in adjacent double well potentials. The combined result of these two tunneling elements

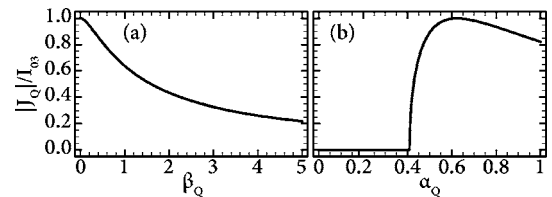


FIG. 5. Circulating current in potential minima for flux bias at the degeneracy point. Magnitude of qubit circulating current  $J_Q$ , as determined by location of potential minimum, is shown as a function of (a)  $\beta_Q$  and (b)  $\alpha_Q$ . Parameters are  $\epsilon=0$ ,  $\phi_Q=\pi$  and  $\alpha_Q=0.7$  (a), and  $\beta_Q=0.1$  (b).

is four states: the ground state wave function is a symmetric superposition localized at  $P_0$  and  $P_1$ , with the same phase in the double well containing  $P_2$ ; the first excited state is symmetric at  $P_0$  and  $P_1$ , but changes phase in the double well containing  $P_2$ , resulting in a nodal plane across the segment connecting  $P_0$  and  $P_2$ ; the second excited state is an antisymmetric combination of states at  $P_0$  and  $P_1$ , but the wave function with respect to  $P_0$  and  $P_2$  is symmetric; finally, the third excited state is antisymmetric with respect to  $P_0$ ,  $P_1$ , and  $P_2$ , resulting in a nodal plane across each tunneling barrier.

When  $\beta_Q$  is non-negligible, one must also look perpendicularly to the  $\gamma_a$ - $\gamma_s$  plane, in the  $\gamma_t$  direction, in order to understand the nature of the two computational basis states. Figure 4 shows two slices through the three-dimensional potential space for a large-inductance flux qubit ( $\beta_Q=0.4$ ). It is clear that the minima do not lie exactly in the  $\gamma_a$ - $\gamma_s$  plane, but actually above and below it in  $\gamma_t$ . Recalling that  $\gamma_t$  is proportional to the circulating current  $J_Q$ , we see that  $P_0$  and  $P_1$  correspond to circulating currents in opposite directions. For the parameters listed in the caption to Fig. 4, the minima lie at  $\gamma_t = \pm 0.2205$ ; for comparison, a circulating current of  $J_Q = \pm I_{03}$ , the magnitude of the critical current of the small junction, would correspond to  $\gamma_t = \pm \alpha_Q \beta_Q (1 + 2\alpha_Q - \kappa_Q^2) / (1 + 2\alpha_Q)(\kappa_Q^2 - 1) = \pm 0.2400$ . The magnitude of the circulating current, as a function of  $\beta_Q$  is shown in Fig. 5(a). We see that estimating the magnitude of the circulating current to be equal to the critical current of the small junction is appropriate for low inductance flux qubits; however, the addition of loop inductance reduces the magnitude of the circulating current in this classical analysis.

In general, for  $\alpha_Q$  less than some critical value, the potential is a single well so that no persistent current can be sup-

ported, rendering the device unsuitable as a qubit. For a qubit with vanishing inductance ( $\beta_Q \rightarrow 0$ ), this critical value is  $\alpha_Q = 1/2$ ; however, as the inductance is increased, a smaller value of  $\alpha_Q$  can support a persistent current. For example, for  $\beta_Q = 0.1$ , the potential is bifurcated at  $\alpha_Q \approx 0.41$  [Fig. 5(b)]. For  $\alpha_Q > 1$  a double well potential still exists, but the barrier to intercell tunneling is lower than the barrier to intracell tunneling. This leads to quantum states of the system which are not suitable for a conventional qubit.

### III. DERIVATION OF THE HAMILTONIAN

To understand fully the dynamics and quantum states of the three junction flux qubit, we must introduce the kinetic energy and form the Hamiltonian. Kinetic energy in the system arises from charges on the junction capacitance, and can be written as

$$T = \Phi_0^2 / (8\pi^2) \times [(C_1 + C_s)\dot{\gamma}_1^2 + (C_2 + C_s)\dot{\gamma}_2^2 + (C_3 + C_s)\dot{\gamma}_3^2]. \quad (12)$$

Here, we have associated a capacitance  $C_i$  with each junction, which we take to be proportional to the critical current and hence the area of the corresponding junction, and a stray capacitance  $C_s$ , which is taken to be the same for all junctions. Equation (12) is of the form  $C_i V_i^2 / 2$ , where the voltage developed across each junction is  $V_i = (\Phi_0 / 2\pi) d\gamma_i / dt$ .

When we apply the coordinate transformations [Eqs. (7)–(9)] and parameter transformations [Eqs. (4)–(6)] defined above, the kinetic energy takes the form

$$T = \frac{\hbar^2}{8E_c} [\dot{\gamma}_a \quad \dot{\gamma}_s \quad \dot{\gamma}_t] \cdot \begin{bmatrix} 1 + \sigma_Q & -\kappa_Q & -\kappa_Q \\ -\kappa_Q & 1 + 2\alpha_Q + 3\sigma_Q & \sigma_Q(\alpha_Q - 1)/\alpha_Q \\ -\kappa_Q & \sigma_Q(\alpha_Q - 1)/\alpha_Q & (\alpha_Q + 2\alpha_Q^2 + \sigma_Q + 2\alpha_Q^2\sigma)/2\alpha_Q^2 \end{bmatrix} \cdot \begin{bmatrix} \dot{\gamma}_a \\ \dot{\gamma}_s \\ \dot{\gamma}_t \end{bmatrix}, \quad (13)$$

where we have introduced the charging energy  $E_c = e^2 / (C_1 + C_2)$ , the stray capacitance ratio  $\sigma_Q = 2C_s / (C_1 + C_2)$ , and used a matrix notation to represent all the terms. Note that the mass tensor in Eq. (13) becomes diagonal in a qubit with no stray capacitance and no asymmetry ( $\kappa_Q = \sigma_Q = 0$ ).

We now form the Hamiltonian  $\mathcal{H}$  using the standard techniques of classical mechanics.<sup>15,16</sup> First we form the Lagrangian  $\mathcal{L} = T - U$  and then calculate the canonical momenta  $\vec{\mathbf{p}} = (p_a, p_s, p_t)$ . We can write this as the vector equation

$\vec{\mathbf{p}} = \partial \mathcal{L} / \partial \vec{\dot{\gamma}}$ , where  $\vec{\dot{\gamma}} = (\dot{\gamma}_a, \dot{\gamma}_s, \dot{\gamma}_t)$ . The Hamiltonian becomes

$$\mathcal{H} = \vec{\mathbf{p}} \cdot \vec{\dot{\gamma}} - \mathcal{L}, \quad (14)$$

which can be expressed as

$$\mathcal{H} = \vec{\mathbf{p}} \cdot \vec{\mathbf{M}}^{-1} \cdot \vec{\mathbf{p}} / 2 + U, \quad (15)$$

where the inverse mass matrix is

$$\vec{\mathbf{M}}^{-1} = 4E_J \{ \hbar^2 [(1 + \sigma_Q)^2 - \kappa_Q^2] \} \times \begin{bmatrix} 1 + \sigma_Q & \frac{\kappa_Q}{1 + 2\alpha_Q} & \frac{2\alpha_Q \kappa_Q}{1 + 2\alpha_Q} \\ \frac{\kappa_Q}{1 + 2\alpha_Q} & \frac{(\sigma_Q + \alpha_Q)(1 + \sigma_Q) + 2\alpha_Q^2(1 - \kappa_Q^2 + 2\sigma_Q + \sigma_Q^2)}{(1 + 2\alpha_Q)^2(\alpha_Q + \sigma_Q)} & \frac{2\alpha_Q[\sigma_Q + \sigma_Q^2 + \alpha_Q(\kappa_Q^2 - \sigma_Q - \sigma_Q^2)]}{(1 + 2\alpha_Q)^2(\alpha_Q + \sigma_Q)} \\ \frac{2\alpha_Q \kappa_Q}{1 + 2\alpha_Q} & \frac{2\alpha_Q[\sigma_Q + \sigma_Q^2 + \alpha_Q(\kappa_Q^2 - \sigma_Q - \sigma_Q^2)]}{(1 + 2\alpha_Q)^2(\alpha_Q + \sigma_Q)} & \frac{2\alpha_Q^2[2\alpha_Q(1 + \sigma_Q) + 1 + 4\sigma_Q + 3\sigma_Q^2 - \kappa_Q^2]}{(1 + 2\alpha_Q)^2(\alpha_Q + \sigma_Q)} \end{bmatrix}. \quad (16)$$

#### IV. SOLUTION TO THE HAMILTONIAN

To find the quantum mechanical solution to the system, we expand the Hamiltonian operator in a complete set of basis functions. The potential energy is  $2\pi$  periodic in both  $\gamma_a$  and  $\gamma_s$ , while the kinetic energy is quadratic for a qubit without asymmetry or stray capacitance. This suggests that expansion in plane waves is appropriate for these two components.

However, while  $\gamma_t$  also has a quadratic kinetic energy and terms in the potential energy which are periodic, the inductive potential is quadratic in  $\gamma_t$ . This suggests that harmonic oscillator wave functions are more appropriate for the expansion in  $\gamma_t$ ; however the periodic terms may present some difficulty, as they require calculating overlap integrals between sinusoids and exponentially decaying polynomials.

Thus we choose for our basis functions the product state

$$|\psi_{klm}\rangle = |\psi_k^a\rangle |\psi_l^s\rangle |\psi_m^t\rangle, \quad (17)$$

where the first two factors are plane waves

$$|\psi_k^a\rangle = (2\pi)^{-1/2} e^{-ik\gamma_a}, \quad (18)$$

$$|\psi_l^s\rangle = (2\pi)^{-1/2} e^{-il\gamma_s}. \quad (19)$$

The third factor is a simple harmonic oscillator wave function in  $\gamma_t$

$$|\psi_m^t\rangle = \left[ \frac{m_t \omega_t}{2^{2m} \pi \hbar (m!)^2} \right]^{1/4} H_m \left[ \sqrt{\frac{m_t \omega_t}{\hbar}} \gamma_t \right] e^{-m_t \omega_t \gamma_t^2 / 2\hbar}, \quad (20)$$

where  $H_m[\gamma]$  is the  $m$ th degree Hermite polynomial. The effective mass for the harmonic oscillator is

$$m_t = \frac{\hbar^2(\alpha_Q + \sigma_Q)[(1 + \sigma_Q)^2 - \kappa_Q^2](1 + 2\alpha_Q)^2}{8E_c \alpha_Q^2 [(1 + \sigma_Q)(1 + 2\alpha_Q + 3\sigma_Q) - \kappa_Q^2]} \quad (21)$$

and the natural frequency is

$$\omega_t = (2E_J \hbar) \times \sqrt{\frac{2E_J \alpha_Q (1 - \kappa_Q^2) [(1 + \sigma_Q)(1 + 2\alpha_Q + 3\sigma_Q) - \kappa_Q^2]}{E_c \beta_Q (1 + 2\alpha_Q - \kappa_Q^2)(\alpha_Q + \sigma_Q) [(1 + \sigma_Q)^2 - \kappa_Q^2]}}. \quad (22)$$

We need to calculate the matrix elements

$$\vec{\mathbf{H}}_{klmk'l'm'} = \langle \psi_{klm} | \mathcal{H} | \psi_{k'l'm'} \rangle. \quad (23)$$

To do this we first Fourier transform the potential energy with respect to  $\gamma_a$  and  $\gamma_s$  and write it as

$$U = E_J \sum_{k=-2}^2 \sum_{l=-1}^1 \vec{\mathbf{U}}_{kl} e^{-i(k\gamma_a + l\gamma_s)} + \frac{1}{2} m_t \omega_t^2 \gamma_t^2, \quad (24)$$

where  $\vec{\mathbf{U}}$  is a function of  $e^{i\gamma_t}$  and  $\phi_Q$

$$\vec{\mathbf{U}}_{kl} = \frac{1}{2} \begin{bmatrix} 0 & (1 - \kappa_Q) e^{i\gamma_t} & 0 & (\kappa_Q - 1) e^{-i\gamma_t} & 0 \\ \alpha_Q e^{i\left(\phi_Q - \frac{\gamma_t}{\alpha_Q}\right)} & 0 & 0 & 0 & \alpha_Q e^{-i\left(\phi_Q - \frac{\gamma_t}{\alpha_Q}\right)} \\ 0 & (\kappa_Q - 1) e^{-i\gamma_t} & 0 & (1 - \kappa_Q) e^{i\gamma_t} & 0 \end{bmatrix}. \quad (25)$$

Note that the  $\vec{\mathbf{U}}_{00}$  component is in the middle of the matrix.

We can now write down the Hamiltonian expansion and address the terms individually

$$\begin{aligned} \vec{\mathbf{H}}_{klmk'l'm'} = & \sum_{\substack{i=\{a,s\} \\ j=\{a,s\}}} \frac{1}{2} \langle \psi_k^a | \langle \psi_l^s | p_i \vec{\mathbf{M}}_{ij}^{-1} p_j | \psi_{l'}^s \rangle | \psi_{k'}^a \rangle + (\vec{\mathbf{M}}_{at}^{-1} \langle \psi_k^a | p_a | \psi_{k'}^a \rangle + \vec{\mathbf{M}}_{as}^{-1} \langle \psi_l^s | p_s | \psi_{l'}^s \rangle) \langle \psi_m^t | p_t | \psi_{m'}^t \rangle \\ & + E_J \sum_{p=-2}^2 \sum_{q=-1}^1 \langle \psi_m^t | \vec{\mathbf{U}}_{pq} | \psi_{m'}^t \rangle \langle \psi_k^a | \langle \psi_l^s | e^{-i(p\gamma_a + q\gamma_s)} | \psi_{l'}^s \rangle | \psi_{k'}^a \rangle + \langle \psi_m^t | \frac{p_t^2}{2m_t} + \frac{1}{2} m_t \omega_t^2 \gamma_t^2 | \psi_{m'}^t \rangle. \end{aligned} \quad (26)$$

The first term is readily evaluated by replacing the momentum operators  $p_i$  with  $-i\hbar(\partial/\partial\gamma_i)$  and performing the integrals

$$\begin{aligned} & \sum_{\substack{i=\{a,s\} \\ j=\{a,s\}}} \int_{-\pi}^{\pi} \int_{-\pi}^{\pi} \frac{-\hbar^2 \vec{\mathbf{M}}_{ij}^{-1}}{8\pi^2} e^{i(k\gamma_a + l\gamma_s)} \\ & \times (\partial/\partial\gamma_i)(\partial/\partial\gamma_j) e^{-i(k'\gamma_a + l'\gamma_s)} d\gamma_a d\gamma_s \\ & = \hbar^2 (k^2 \vec{\mathbf{M}}_{aa}^{-1}/2 + k l \vec{\mathbf{M}}_{as}^{-1} + l^2 \vec{\mathbf{M}}_{ss}^{-1}/2) \delta_{kk'} \delta_{ll'}, \end{aligned} \quad (27)$$

where we have introduced the Kronecker delta function  $\delta_{ab}$ .

For the second term of Eq. (26), the first factor involving  $p_a$  and  $p_s$  is straightforward to calculate using the same technique as the first term. The second factor, involving  $p_t$ , is evaluated by representing the momentum operator with harmonic oscillator annihilation and creation operators,  $p_t = i\sqrt{m_t\omega_t\hbar}/2(a_t^\dagger - a_t)$

$$\begin{aligned} & (\vec{\mathbf{M}}_{at}^{-1} \langle \psi_k^a | p_a | \psi_{k'}^a \rangle + \vec{\mathbf{M}}_{as}^{-1} \langle \psi_l^s | p_s | \psi_{l'}^s \rangle) \\ & \times i\sqrt{\frac{m_t\omega_t\hbar}{2}} (\langle \psi_m^t | a_t^\dagger | \psi_{m'}^t \rangle - \langle \psi_m^t | a_t | \psi_{m'}^t \rangle) \\ & = -i\sqrt{\frac{m_t\omega_t\hbar^3}{2}} (\vec{\mathbf{M}}_{at}^{-1} k \delta_{kk'} + \vec{\mathbf{M}}_{as}^{-1} l \delta_{ll'}) \\ & \times (\sqrt{m+1} \delta_{m',m+1} - \sqrt{m} \delta_{m',m-1}). \end{aligned} \quad (28)$$

Evaluating the third set of terms of Eq. (26) involves calculating two factors. The second factor is simply another plane wave overlap integral, giving

$$\langle \psi_k^a | \langle \psi_l^s | e^{-i(p\gamma_a + q\gamma_s)} | \psi_{l'}^s \rangle | \psi_{k'}^a \rangle = \delta_{k,p+k'} \delta_{l,q+l'}. \quad (29)$$

The first factor involves overlap integrals between harmonic oscillator wave functions and exponentials. The formula required to evaluate this factor is<sup>17</sup>

$$\begin{aligned} \langle \psi_m^t | e^{k\gamma_t} | \psi_{m'}^t \rangle & = (m!m')^{-1/2} e^{\frac{\hbar k^2}{4m_t\omega_t}} \sum_{j=0}^{\min\{m,m'\}} j! \binom{m}{j} \binom{m'}{j} \\ & \times \left( \frac{\hbar k^2}{2m_t\omega_t} \right)^{(m+m'-2j)/2}. \end{aligned} \quad (30)$$

The final term of Eq. (26) is easy to understand. It is simply the overlap of a harmonic oscillator Hamiltonian with harmonic oscillator basis functions, giving

$$\langle \psi_m^t | \frac{p_t^2}{2m_t} + \frac{1}{2} m_t \omega_t^2 \gamma_t^2 | \psi_{m'}^t \rangle = \left( m + \frac{1}{2} \right) \hbar \omega_t \delta_{mm'}. \quad (31)$$

Thus, all the matrix elements in  $\vec{\mathbf{H}}_{klmk'l'm'}$  can be written down in closed form. The matrix is infinite dimensional in this basis, but we can truncate it for numerical diagonalization by letting  $k$  and  $k'$  run from  $-n_k$  to  $n_k$ ,  $l$  and  $l'$  run from  $-n_l$  to  $n_l$ , and  $m$  and  $m'$  run from 0 to  $n_m$ . The eigenvalues of  $\vec{\mathbf{H}}$  then give the energy levels and the eigenvectors give the coefficients of the wave functions. Experience has shown that  $(n_k, n_l, n_m) = (5, 10, 2)$  gives good results for small inductance flux qubits, say  $\beta_Q < 0.1$ , since the addition of more basis functions affects both the intracell and intercell splittings by less than 1%. For larger values of  $\beta_Q$ ,  $n_m$  must be increased to capture the effect of the inductance.

In Fig. 6(a) we show the result of such a numerical calculation, with the flux bias running over its period of  $\Phi_0$ . We see that when the flux bias is near an integer the energy levels disperse parabolically, as  $U_l$  increases quadratically. Where energy levels cross, tunneling matrix elements lift the degeneracy, resulting in gaps. Near a flux bias of  $\Phi_0/2$  a double well potential forms, resulting in inverted dispersion curves. At  $\Phi_Q = \Phi_0/2$  the wave functions consist of symmetric and antisymmetric combinations of localized states at  $P_0$  and  $P_1$  (Fig. 3). These two states can be further symmetrized or antisymmetrized by the tunneling element connecting  $P_0$  to  $P_2$ , resulting in a fine splitting for each energy level. Due to this intercell tunnel coupling, all of the energy levels are actually doublets with splittings at the degeneracy point between 100 kHz and 1 MHz, too small to be resolved on the scale of Fig. 6(a) and smaller than the presently achieved spectroscopic linewidths in flux qubit measurements.<sup>5-7</sup> Thus the level splitting which is measured at  $\Phi_Q/\Phi_0 = 0.5$ ,  $\Delta$  or the intracell splitting, is actually the energy difference between the ground state and the *second* excited state; transitions between the ground and first excited states, and between the second and third excited state, give the energy of intercell splittings. At  $\Phi_Q/\Phi_0 = 0.5$ , although the ground and first excited states are separated by the intercell tunnel splitting, these states are macroscopically indistinguishable. As  $\Phi_Q$  is moved away from  $\Phi_0/2$ , this intercell splitting decreases rapidly [Fig. 6(b)] as the tunneling probability between neighboring cells vanishes and the intracell dynamics dominates.

Figure 7 shows a series of numerical calculations of the qubit energy levels for different values of  $\beta_Q$ . As  $\beta_Q$  increases the spacing between the ground and second excited state decreases, while the higher excited states are elevated to

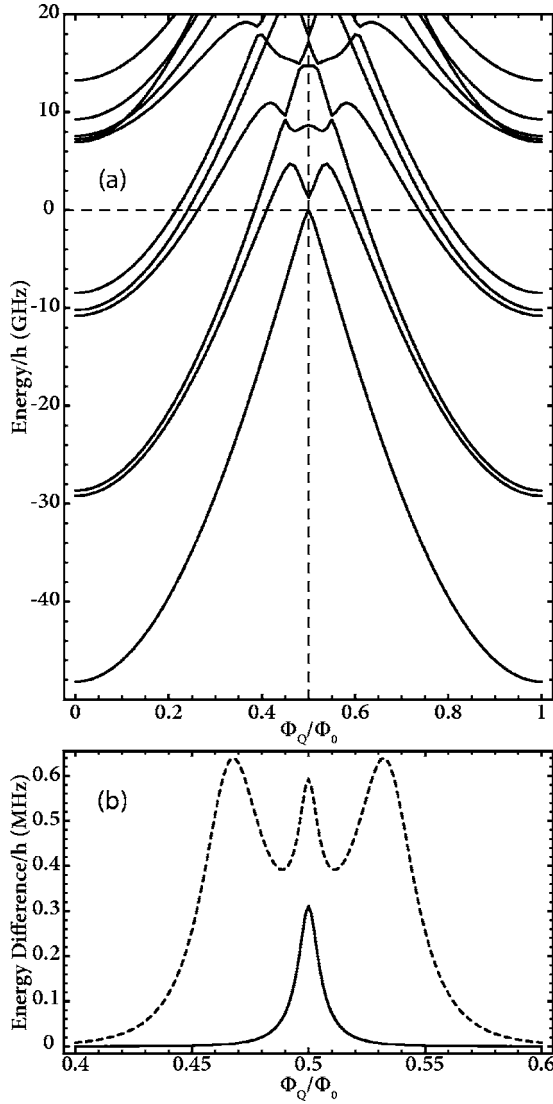


FIG. 6. (a) Calculated energy levels of the three-junction flux qubit as a function of  $\Phi_Q$  for  $\beta_Q=0.15$ ,  $\alpha_Q=0.63$ ,  $\kappa_Q=0$ ,  $\sigma_Q=0$ ,  $E_J/h=50$  GHz,  $E_C/h=1$  GHz,  $n_k=5$ ,  $n_l=10$ , and  $n_m=2$ . Each visible line is actually a doublet split by the intercell tunneling. (b) Flux dependence of the intercell splitting between the ground and first excited states (solid) and second and third excited states (dashed) for the same device parameters.

larger energies. The states of opposite circulating current can be identified by the way they disperse hyperbolically in opposite directions. The difference in energy between these states fits quite well to the hyperbolic form  $\delta E = \sqrt{\Delta^2 + \epsilon^2}$ ,

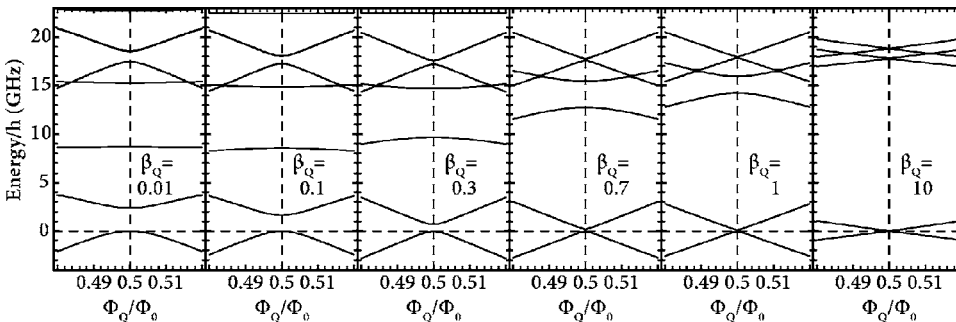


FIG. 7. Calculated energy levels of the three-junction flux qubit for six different values of  $\beta_Q$ : {0.01, 0.1, 0.3, 0.7, 1, 10}. Each plot shows energy as a function of  $\Phi_Q$  for  $\alpha_Q=0.63$ ,  $\kappa_Q=0$ ,  $\sigma_Q=0$ ,  $E_J/h=50$  GHz,  $E_C/h=1$  GHz,  $n_k=5$ ,  $n_l=10$ , and  $n_m=2$ . Each visible line is actually a doublet split by the intercell tunneling.

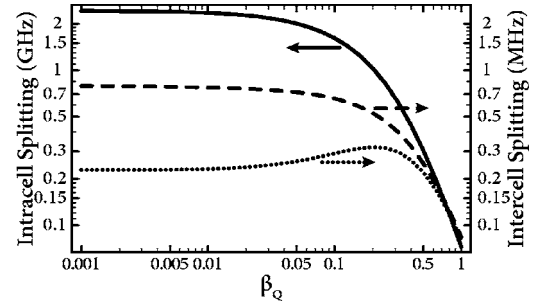


FIG. 8. Calculated tunnel splittings as a function of  $\beta_Q$  for three-junction flux qubit. Parameters are  $\alpha_Q=0.63$ ,  $\kappa_Q=0$ ,  $\sigma_Q=0$ ,  $E_J/h=50$  GHz,  $E_C/h=1$  GHz,  $\Phi_Q=\Phi_0/2$ ,  $n_k=5$ ,  $n_l=10$ , and  $n_m=6$ . Solid curve, associated with left axis, corresponds to intracell tunneling frequency for transition between ground state and second excited state  $\Delta$ . Right axis shows intercell tunneling frequency for transition between ground and first excited state (dotted curve), and between second and third excited states (dashed curve).

where  $\epsilon$  is proportional to  $\Phi_Q - \Phi_0/2$ ; the root-mean-square (rms) deviation is less than 20 MHz, indicating that a three-junction flux qubit truncated to these two states is well approximated as an ideal two state system.

Using the numerical techniques described above, we studied the variation of the intracell splitting  $\Delta$  for typical three-junction flux qubit parameters as  $L_Q$  is varied. Figure 8 contains a plot of  $\Delta$  versus  $\beta_Q$ . For small  $\beta_Q$ ,  $L_Q$  has a negligible effect on  $\Delta$ . However, as  $\beta_Q$  approaches 1, which corresponds to a loop inductance  $L_Q=11.8$  nH for the parameters in Fig. 8,  $\Delta$  drops by more than an order of magnitude, rendering the device no longer useful as a qubit. However, keeping  $\beta_Q$  below  $\sim 0.2$  corresponds to a substantial value of  $\Delta$  ( $>1$  GHz), while allowing for a loop inductance as large as 2 nH, sufficient for most proposed scalable biasing<sup>6</sup> and qubit coupling schemes.<sup>10</sup> Figure 8 also shows the effect of the intercell splittings at  $\Phi_Q=\Phi_0/2$ . Note that the intercell splitting in the small- $\beta_Q$  limit is approximately  $10^4$  times smaller than the intracell splitting, consistent with a previous calculation for a small- $\beta_Q$  qubit.<sup>11</sup> The intercell splittings remain approximately constant as  $\beta_Q$  is increased, until they begin to drop precipitously with the intracell splitting around  $\beta_Q=0.3$ .

We investigated the effect of asymmetry between the two large qubit junctions by calculating the energy levels for different  $\kappa_Q$  (Fig. 9). As  $\kappa_Q$  is increased,  $\Delta$  decreases, although the essential nature of the qubit is preserved. This behavior is summarized in Fig. 10 where we plot  $\Delta$  versus  $\kappa_Q$ . For the parameters used in this plot, there is a cusp at  $\kappa_Q=0.37$  cor-

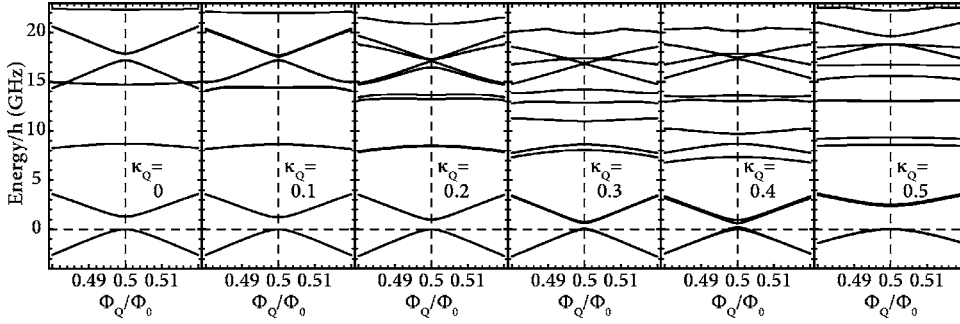


FIG. 9. Calculated energy levels of the three-junction flux qubit for five different values of  $\kappa_Q$  ranging from 0 to 0.5. Each plot shows energy as a function of  $\Phi_Q$  for  $\alpha_Q=0.63$ ,  $\beta_Q=0.15$ ,  $\sigma_Q=0$ ,  $E_J/h=50$  GHz,  $E_C/h=1$  GHz,  $n_k=5$ ,  $n_l=10$ , and  $n_m=2$ .

responding to the point  $\kappa_Q + \alpha_Q = 1$ , where  $I_{02} = I_{03}$ . Thus, at this cusp, the smaller of the two strong junctions, with critical current  $I_{02}$ , and the weak junction, with critical current  $I_{03}$ , swap roles. Also shown are the intercell splittings at  $\Phi_Q = \Phi_0/2$ , which increase with  $\kappa_Q$  and are maximal at the cusp where the intercell tunneling barrier is lowest. Based on the plot in Fig. 10, if one maintains  $\kappa_Q$  below  $\sim 0.1$ ,  $\Delta$  will be minimally affected and the intercell splittings will remain small. A value of  $\kappa_Q = 0.1$  corresponds to a 22% asymmetry in the critical currents of junctions 1 and 2, well within the capabilities of conventional nanofabrication techniques.

As a practical matter, the effect of stray capacitance, as captured by the parameter  $\sigma_Q$ , may be important for a quantitative understanding of the three-junction flux qubit. Since a submicron junction has a capacitance of only a few femtofarads, the contributions from stray capacitance may be non-negligible. The main effect of such stray capacitance is to reduce the spacing between energy levels, just as a corresponding decrease in  $E_c$  would. A secondary effect is that the effective ratio of the capacitances between the small and large junctions increases as  $\sigma_Q$  increases, resulting in behavior similar to an increase in  $\alpha_Q$ .

## V. CONCLUDING REMARKS

Flux qubits with non-negligible loop inductance are desirable for coupling to on-chip flux bias lines to build scalable

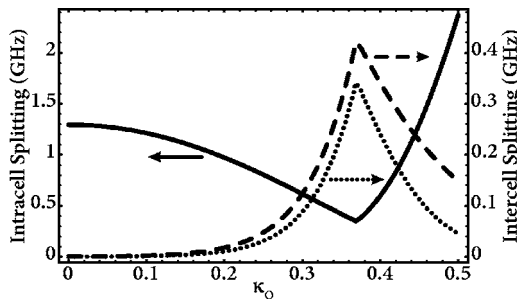


FIG. 10. Calculated tunnel splitting  $\Delta$  as a function of  $\kappa_Q$  for three-junction flux qubit. Parameters are  $\alpha_Q=0.63$ ,  $\beta_Q=0.15$ ,  $\sigma_Q=0$ ,  $E_J/h=50$  GHz,  $E_C/h=1$  GHz,  $\Phi_Q=\Phi_0/2$ ,  $n_k=5$ ,  $n_l=10$ , and  $n_m=2$ . Solid curve, associated with left axis, corresponds to intracell tunneling frequency for transition between ground state and second excited state. Right axis shows intercell tunneling frequency for transition between ground and first excited state (dotted curve), and between second and third excited states (dashed curve). Note the cusp occurs at  $\alpha_Q + \kappa_Q = 1$ , demonstrating the interplay between these parameters.

architectures and for providing the interactions between qubits necessary for generating entanglement. Thus, it is crucial to understand the effects of the loop inductance on the behavior of flux qubits. Furthermore, the effects of asymmetry due to realistic variations in junction fabrication must be accounted for to make predictions of the qubit energy levels for a given chip design. To advance these goals, we have studied the energy levels of the three-junction flux qubit in the full three-dimensional treatment. In the limit of vanishing  $\beta_Q$ , the qubit dynamics can be well approximated by a two-dimensional model in the plane of zero-inductive energy. However, for larger  $\beta_Q$ , when the loop inductance is no longer negligible compared to the Josephson inductance, the minima of the potential energy move away from the zero-inductive energy plane; one must account for this shift in determining the tunnel coupling between the wells. To capture these inductive effects, we constructed three-dimensional wave functions consisting of plane waves and harmonic oscillator modes, and solved numerically for the eigenvalues of the qubit Hamiltonian.

We computed the resulting energy levels as the qubit parameters were varied. For a flux bias  $\Phi_Q$  near  $0.5\Phi_0$ , the dispersion of the ground and second excited states—after the doublet splitting due to intercell tunneling has been taken into account—exhibited the expected hyperbolic dependence. As we increased  $\beta_Q$  this hyperbolic dispersion persisted, but the gap  $\Delta$  between the ground and second excited states at  $\Phi_Q = 0.5\Phi_0$  decreased substantially and the higher energy levels became distorted and were elevated to larger energies. As  $\beta_Q$  approached unity,  $\Delta$  decreased by more than an order of magnitude.

We also investigated the effect of junction asymmetries on the qubit energy levels. As the asymmetry  $\kappa_Q$  between the two large junctions was increased, the dispersion of the ground and second excited states continued to follow the hyperbolic form, but  $\Delta$  was suppressed somewhat while the intercell tunnel splittings were enhanced.

We conclude that the three-junction flux qubit is a versatile device that can accommodate substantial amounts of loop inductance, enabling scalable biasing schemes and interqubit couplings, and moderate asymmetry between the junctions, as is typical of current fabrication processes. However, to predict the resulting energy levels, one must consider the full three-dimensional problem. Furthermore, the inductance and asymmetry should not be increased to arbitrarily large values, as  $\Delta$  would be suppressed substantially, rendering the device no longer useful as a qubit.

## ACKNOWLEDGMENTS

We thank Joel Moore for stimulating discussions and Franco Nori, Yasunobu Nakamura, and Frank Wilhelm for their thoughtful comments on our manuscript. This work was

supported by the Air Force Office of Scientific Research under Grant No. F49-620-02-1-0295, the Army Research Office under Grant No. DAAD-19-02-1-0187, the National Science Foundation under Grant No. EIA-020-5641, and the Advanced Research and Development Activity.

\*Current address: Proteus Biomedical, 750 Chesapeake Drive, Redwood City, CA 94063.

†Current address: Department of Physics, Syracuse University, Syracuse, NY 13244-1130.

‡Current address: Physics Department, National Tsing Hua University.

<sup>1</sup>A. J. Leggett and A. Garg, *Phys. Rev. Lett.* **54**, 857 (1985).

<sup>2</sup>J. R. Friedman, V. Patel, W. Chen, S. K. Tolpygo, and J. E. Lukens, *Nature (London)* **46**, 43 (2000).

<sup>3</sup>J. E. Mooij, T. P. Orlando, L. S. Levitov, L. Tian, C. H. van der Wal, and S. Lloyd, *Science* **285**, 1036 (1999).

<sup>4</sup>C. H. van der Wal, A. C. J. ter Haar, F. K. Wilhelm, R. N. Schouten, C. J. P. M. Harmans, T. P. Orlando, S. Lloyd, and J. E. Mooij, *Science* **290**, 773 (2000).

<sup>5</sup>S. Saito, M. Thorwart, H. Tanaka, M. Ueda, H. Nakano, K. Semba, and H. Takayanagi, *Phys. Rev. Lett.* **93**, 037001 (2004).

<sup>6</sup>B. L. T. Plourde, T. L. Robertson, P. A. Reichardt, T. Hime, S. Linzen, C.-E. Wu, and J. Clarke, *Phys. Rev. B* **72**, 060506(R) (2005).

<sup>7</sup>I. Chiorescu, Y. Nakamura, C. J. P. M. Harmans, and J. E. Mooij, *Science* **299**, 1869 (2003).

<sup>8</sup>E. Ilichev, N. Oukhanski, A. Izmalkov, T. Wagner, M. Grajcar, H. G. Meyer, A. Smirnov, A. Maassen van den Brink, M. H. S. Amin, and A. M. Zagoskin, *Phys. Rev. Lett.* **91**, 097906 (2003).

<sup>9</sup>G. J. Dolan, *Appl. Phys. Lett.* **31**, 337 (1977).

<sup>10</sup>B. L. T. Plourde, J. Zhang, K. B. Whaley, F. K. Wilhelm, T. L. Robertson, T. Hime, S. Linzen, P. A. Reichardt, C.-E. Wu, and J. Clarke, *Phys. Rev. B* **70**, 140501(R) (2004).

<sup>11</sup>T. P. Orlando, J. E. Mooij, L. Tian, C. H. van der Wal, L. Levitov, S. Lloyd, and J. J. Mazo, *Phys. Rev. B* **60**, 15398 (1999).

<sup>12</sup>D. S. Crankshaw and T. P. Orlando, *IEEE Trans. Appl. Supercond.* **11**, 1006 (2001).

<sup>13</sup>A. Maassen van den Brink, *Phys. Rev. B* **71**, 064503 (2005).

<sup>14</sup>J. Q. You, Y. Nakamura, and F. Nori, *Phys. Rev. B* **71**, 024532 (2005).

<sup>15</sup>H. Goldstein, *Classical Mechanics*, 2nd ed. (Addison-Wesley, Reading, MA, 1980).

<sup>16</sup>J. José and E. Saletan, *Classical Dynamics: A Contemporary Approach* (Cambridge University Press, Cambridge, England, 1998).

<sup>17</sup>W. Witschel, *Eur. J. Phys.* **17**, 357 (1996).